Working together for a green, competitive and inclusive Europe

# Toward Large Area Perovskite Solar Cells (PERLA-PV)





**WP1 and WP2 – Preparation of standard and inverted PSCs**

Printing technologies

Composition and solvent engineering

Small and large PSCs

5x5 cm²

5x5 cm²
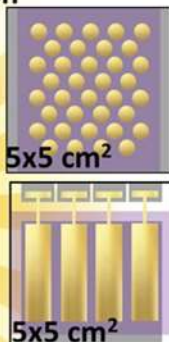
**WP3/WP4 – Modelling of materials and interfaces/Device characterization and modelling**

Proper materials

Optimal interfaces

m-DEM

Enhanced PCE

Degradation processes and hysteresis
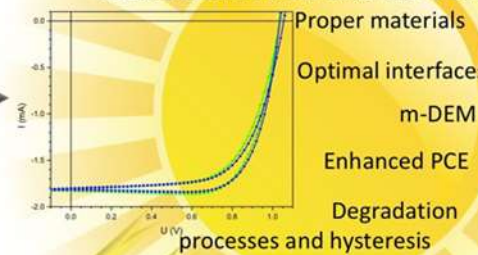
**WP5 – Device encapsulation, panels production**

15 cm

15 cm
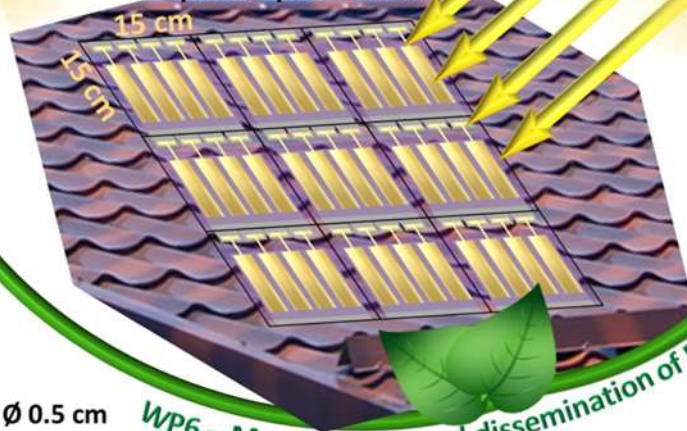
Au

FTO

TiO₂/Perovskite/ spiro-OMeTAD

Active area  Ø 0.5 cm

Active area  0.8 x 3 cm

WP6 – Management and dissemination of PERLA PV

2022

The **PERLA-PV** project started in 2021. It addresses the development of efficient large area perovskite solar cells (PSC) and photovoltaic modules using cheap and environmental friendly technologies. Based on certified record values, as-grown (unstabilized) small area PSCs achieved a power conversion efficiencies over 25%, outperforming some types of Si solar cells, CdTe and CIGS cells. Being also inexpensive to produce, thin, light and suitable for fabrication with printing technologies the PSCs have in principle a great potential for large scale applications and commercialisation. The consortium is composed by 5 partners: project promotor PP - National Institute of Materials Physics (NIMP), P3- *Horia Hulubei National Institute for R&D in Physics and Nuclear Engineering* (IFIN-HH) and P4 - Tritech Group (WATTROM), a SME as end-user, all from Romania; P1- Oslo University (UiO) from Norway and P2 -Reykjavik University (RU) from Iceland. Each partner is bringing valuable added value to the project in terms of expertise and available experimental techniques. PP is bringing the expertise in the field of chemical deposition methods, in producing PSCs, and in developing low cost deposition printing techniques; P1 has a solid expertise in deposition of inorganic oxide thin films and in characterization of functional materials by various techniques; P2 has expertise in DFT and molecular dynamics as well as in modelling transport properties in complex structures; P3 has an extraordinary expertise on data processing using high performance computing; P4 is a SME with experience in manufacturing and commercialization of photovoltaic modules and systems.

The main research activities employed by each partner are shortly described below:
**PP-NIMP:**
- synthesis, deposition and chemistry optimization of the component layers in PSCs structures; that is including different electron transporter materials ($TiO_2$ and $SnO_2$) and compositional engineering of the halide perovskite material.
- advanced chemical, structural and optical analyses (XRD, SEM, Raman, AFM, FTIR)
- development of the printing technnology and of the chemical methods to prepare the precursor materials; solvent engineering needed for passing from small area spin-coating technique to the deposition of the perovskite layer using large area techniques (slot-die) were the use of anti-solvents is not possible anymore. Two different printing methods are used, the spray deposition for the ETL oxide films and slot die for depositing the perovskite and organic layers in PSC structures
- fabrication of small and large area standard and inverted PSCs
- electrical and photovoltaic characterization of small and large areas PSCs, a necessary step to provide experimental quantities necessary as inputs for theoretical modelling (J-V characteristics, EQE, PCE, impedance spectroscopy)
- in addition to the role envisaged in the project, PP addressed also the deposition of Cu and Ni oxides by sputtering.

**P1 - UiO**:
- Synthesis of oxide films used as HTM in the inverted PSC devices, $CuO_x$ and Cu:NiO;
- Structural and chemical characterization of the Cu and Ni oxides (XRD, FTIR, Hall measurements, resistivity)

**P2-RU** – DFT calculations to describe the band alignment at the new perovskite/ETM interface (e.g. $SnO_2$ as ETM) and a characterization of the $TiO_2$/$SnO_2$ interface

Iceland
Liechtenstein
Norway grants

ue-fiscdi
Executive Agency for Higher
Education, Research, Development
and Innovation Funding

- DFT calculations to describe the band alignment at the interface between the perovskite and the inorganic HTM (e.g. $Cu_2O$, other transition metal oxides).
- Modelling iodine migration in the HP layer using molecular dynamics. Force field parametrizations from DFT calculations used as input for molecular dynamics codes (LAMMPS).

**P3-IFIN-HH:**
– modelling of dynamic characteristics of both standard and inverted structures
- Comprehensive study of hysteresis phenomena in perovskite solar cells
- Identification of the most probable degradation mechanism, correlation with the hysteresis behavior and negative capacitance measured at low frequencies
- Development of a measurement protocol for correct determination of PCE and its degradation

**P4-WATTROM:**
- Contributes with its expertise on encapsulating, modules fabrication and testing procedures
- elaborate encapsulation procedures for small and large area PSCs produced by PP
- perform the encapsulation and design the degradation tests


**Research and Results in 2022**

| Explanation of the work carried out by the participants |
|---|
| Below we describe the work carried out by the participants in 2022 according to the EEA 36 project, workpackages (WP) and tasks (T):<br><br>**WP1: Preparation of standard PSCs**<br><br>*PP (NIMP) and P1 (UiO) has worked on:*<br><br>**T 1.2.** <u>Perovskite preparation by using solvent engineering</u>, with the role to control the morphology of the perovskite film and to avoid the use of non-friendly solvents.<br>As a good solubilisation of Pb halides used in halide perovskite preparation is only possible with polar solvents, we have studied the replacement of the most toxic one, dimethylformamide (DMF) with less toxic alternatives, such as N-methyl-2-Pyrrolidone (NMP) and ethyl acetate (EA). Also, by employing solvent engineering, we succeed the deposition of perovskite layer by slot die printing technique *without using any anti-solvent*.<br><br>**T 1.3.** <u>Compositional engineering</u> (**PP**)<br>The studies started in 2021 from the $CH_3NH_3PbI_3$ (MAPI) with compositional engineered HP double perovskites continued in 2022. We also investigate the effect of partial substitution of Pb in $MAPbI_{2.6}Cl_{0.4}$ hybrid perovskite with non-toxic alkaline earth metal ions ($Mg^{2+}$) and transition metal ions ($Zn^{2+}$). Microstructural and optical properties of the prepared samples were analyzed by XRD, SEM, AFM, and UV-Vis.<br><br>**T 1.5.** <u>HTM engineering. prepare, deposit and characterize the hole transporter layer:</u><br> *(1) organic,* SpiroOMeTAD on all fabricated standard PSCs (**PP**) and **additional to what was foreseen for PP in the project** *(2) inorganic* based on Cu oxides deposited by reactive radio-frequency magnetron sputtering under different deposition conditions. Specific to (2), modifications of the RF-MS system were performed, by implementing a new magnetron |

Iceland
Liechtenstein
Norway grants

uefiscdi
Executive Agency for Higher
Education, Research, Development
and Innovation Funding

cathode allowing a noteworthy improvement of the structural uniformity of $CuO_x$ films over large area substrates, an important step towards the translation to large-area PSCs. **P1 (UiO)** has deposited pure $NiO_x$ doped $NiO_x$ films sputtered from a NiO target and by E-beam in low and high oxygen partial pressure on which **PP** made XRD- characterisation of these layers and some of them were integrated in standard PSCs.

**T 1.6.** Fabrication of small and large area standard PSCs. The first slot-die experiments were employed using small FTO/glass substrates of 1.5x2.5 $cm^2$ size. They envisaged the adjustment of deposition parameters for MAPI and FAMA based halide perovskites.such as: temperature of the plate, distance of the blade from the slot-die heated plate, speed of the blade, flow rate of the injected solutions delivered by the pump and thermal treatments. As the work inside the small glow-box was quite difficult and anti-solvent treatment was eliminated, the slot-die system was moved back outside the glow- box (see Fig. 2 below).



*Figure 1.* Slot-die MTI machine with mobile vapor extraction used for fabricating small and large area PSCs (from 0.083 $cm^2$ to 4.5 $cm^2$ active areas).

***Transitioning for spin coating to slot-die deposition***

Spin coating is the most accessible method for lab testing of materials fabricated by wet deposition because of its significant advantages, namely the simple and easy to use apparatus and the fine control over the layer thickness. Still, it presents two major drawbacks: inability to deposit large area films and high material waste. This is due to the operating principle of the method itself: a precursor solution is spread by the centrifugal force creating by spinning the substrate using an electric motor with fine speed and time control, any excess being pushed to the side and removed. The film is formed by the wetting of the substrate with the precursor solution. Due to this a large amount of material is lost. The deposition area is limited by the balance between the superficial tension of the liquid on the sample surface and the tangential speed that increases when we move away from the center of the sample. Also, because of the same reason, the deposited film may present thickness inequalities even on the continuous zones. The main reason for transitioning to a slot-die method is the desire to fabricate large area films. This comes with multiple difficulties. Some information gleaned from experiments using spin coating are useful (like solution composition and preparation, crystallization temperatures or thickness requirements) but a lot of new parameters have to be determined.

Slot-die is large area deposition method that uses a head to deposit a precursor ink on to the substrate by forming a meniscus between the head and the surface. As the slot-die head is moved by the system a wet film is formed on the substrate surface and the final film is obtained by applying a thermal treatment during or after the deposition. Multiple parameters are responsible for the film formation: ink rheological properties, composition and pump speed, slot-die head opening and speed, slot-die head to substrate height, surface morphology and wetting angle and the thermal treatment used. The slot-die method is similar to the dr. blade method, but instead of having a blade which levels the ink placed in front of the blade, a head with an internal reservoir is used which has the advantage of a controlled flow of ink as the reservoir is supplied by a pump system. Because of this the slot-die deposition technique requires the use of low viscosity inks, the use of high viscosity inks (pastes) being feasible only with dr. blade. Irrespective of the method thin film (up to a minimum of tens of nm) are possible. All enumerated parameters have a degree of influence on the final film thickness, careful selection and control being required.

## WP2: Preparation of inverted PSCs

**T 2.1.** Deposition, characterization and optimization of compositional engineered HP **(PP-NIMP)**.  Three types of HP compositions were investigated:
*(i)* one composition very close to the most basic $MAPbI_3$ with a small quantity of $Cl^-$, $MAPbI_{2.6}Cl_{0.4}$, *(MAPICl)*, we consider it the "starting composition";
(ii) incorporation of 10% $K^+$ incorporation and partial substitution of $FA^+$, resulting the composition: $FA_{0.7}K_{0.1}MA_{0.2}PbI_{2.8}Cl_{0.2}$, *(FAMA10K)*;
(iii) one composition with another halogen in higher quantity, $Br^-$, $MAPbI_{1.8}Br_{1.2}$ , (*MAPIBr*). They were optimized for integration in PSCs depositing above the perovskite PCBM as ETL**.**

**T 2.2.** Deposition and characterisation of inorganic HTM (**P1-UiO and PP-NIMP**)
**P1** had deposited $NiO_x$ films sputtered from a NiO target and by E-beam in low and high oxygen partial pressure and **PP** made XRD- characterisation of these layers.

**T 2.3.** Deposition and characterization of PCBM layer acting as ETM (**PP-NIMP**)
PCBM with or without BCP was deposited and characterize as ETM. PCBM, was prepared by dissolving different amounts in CB (clorbenzene), and spincoated at 1500 RPM/ 30s/ 2000RPM/ 15s. BCP was either spincoated at 2000 RPM/ 30s from a saturated solution in methanol filtered (PTFE 0.45µm) or by thermal evaporation. The three perovskite compositions mentioned at **T 2.1.** The three compositions mentioned at **T 2.1** were used as photoactive layers in inverted solar cells, using PEDOT:PSS as p-type layer and PCBM  with or without BCP (bathocuproine) as n-type layer. A resume of the PCBM optimization results when integrated in the structure of inverted perovskite solar cells with respect of photovoltaic parameters for selected perovskites is given in Table 1.

## Table 1

| Structure of inverted solar cell | PCE, %(max) |
|---|---|
| ITO/ PEDOT:PSS/ $FA_{0.7}K_{0.1}MA_{0.2}PbI_{2.8}Cl_{0.2}$/ PCBM 2,5 mg/ml/ Au | 2.24 |
| ITO/ PEDOT:PSS/ $MAPbI_{2.6}Cl_{0.4}$ / PCBM 2,5 mg/ml/ Au | 0.46 |
| ITO/ PEDOT:PSS/ $FA_{0.7}K_{0.1}MA_{0.2}PbI_{2.8}Cl_{0.2}$/ PCBM 5 mg/ml/ Au | **5.18** |
| ITO/ PEDOT:PSS/ $MAPbI_{2.6}Cl_{0.4}$ / PCBM 5 mg/ml/ Au | 3.24 |
| ITO/ PEDOT:PSS/ $FA_{0.7}K_{0.1}MA_{0.2}PbI_{2.8}Cl_{0.2}$/ PCBM 10 mg/ml/ Au | 1.45 |
| ITO/ PEDOT:PSS/ $MAPbI_{2.6}Cl_{0.4}$ / PCBM 10 mg/ml/ Au | 3.27 |
| ITO/ PEDOT:PSS/ $MAPbI_{1.8}Br_{1.2}$/ PCBM 5mg/ml/ Au | 4.81 |
| ITO/ PEDOT:PSS/ $FA_{0.7}K_{0.1}MA_{0.2}PbI_{2.8}Cl_{0.2}$ / PCBM 4 mg/ml/ BCP/ Au | **6.155** |

**T 2.4.** Production of small and large area inverted PSCs **(PP-NIMP)**
During 2022 both small and large area inverted solar cels were fabricated (e.g. Fig.2.



Back side view (top electrodes)          Front side view (through the substrate)
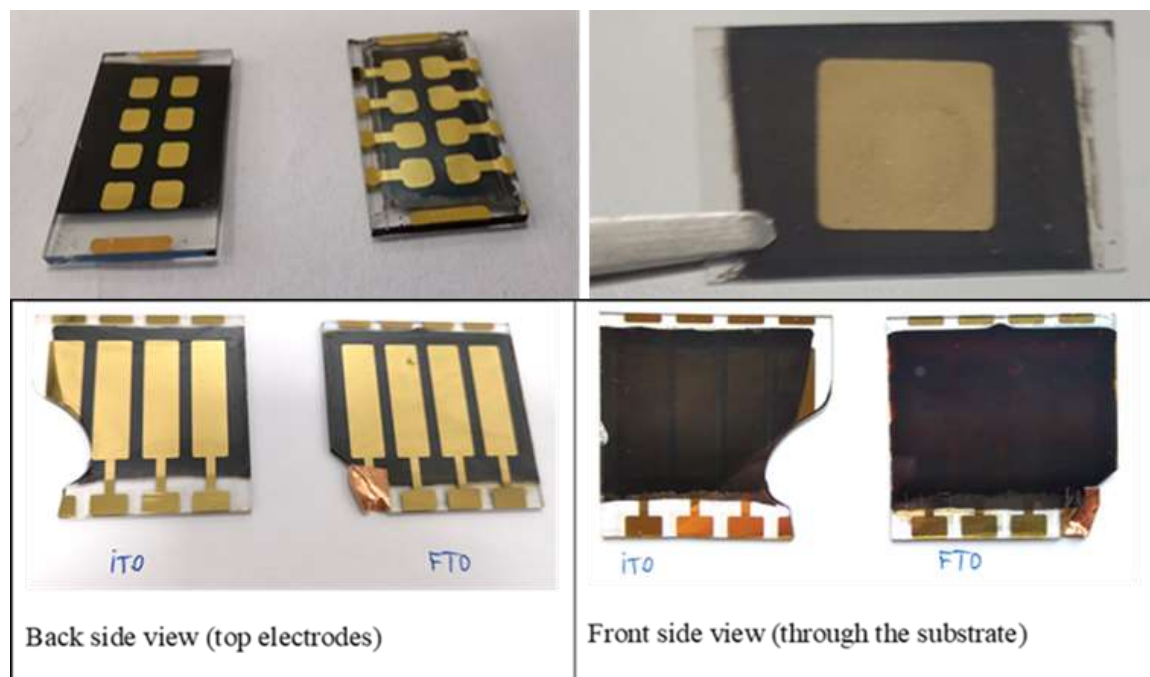
## Figure. 2.

Inverted perovskite solar cells with active area of maximum 1 cm$^2$ were obtained by using either spin-coating or slot-die techniques. Larger active areas up to 4.48 cm$^2$ are obtained only by employing slot-die large area deposition method.

## WP 3: Modelling of materials and interfaces

The theoretical work in 2022 was **jointly performed by P2(RU)** and **P3(NIPNE)** on:

### *T 3.1 - Electronic band structure calculations and stability assessment of new HP candidates*

The studies started in 2021 on MAPbI$_3$ extended in 2022 on structures assembled by tetragonal tin oxide SnO$_2$ and the extended class of perovskites of formula FA$_x$MA$_{1-x}$Pb(I$_y$Cl$_{1-y}$)$_3$, obtained by doping FA$^+$ and Cl$^-$ ions into parental MAPbI$_3$.

### *T 3.2. Assessment of the stability and localization of the interface defect states*

The main issue regarding MAPbI$_3$ material for photovoltaic applications is its lack of stability over time, especially triggered by the iodine (I) migration within the material, ultimately lowering the efficiency over time. Computer simulations of I motion in MAPI were performed while three cases of defects were studied: I vacancies, I interstitial ions, and a combination of them. Molecular dynamics (MD) simulations were performed using the LAMMPS specialized software accounting the movement of all atoms in the material when a defect is present. The displacement of iodine atoms in the lattice has been calculated, as well as the diffusion coefficients of the vacancy and iodide. The results are presented in deliverable D8 in mid-term report.

### *T 3.3 Mapping the electrostatic potential at grain boundaries and describe the interaction with H$_2$O molecules.* The electrostatic potential was calculated using the charge distribution from LAMMPS output data and the effect of water molecules and grain boundaries were evaluated with respect of ion migration. The effect of water molecules was tested with both, MD -by using LAMMPS software, and DFT method- using the SIESTA package. The results are detailed in D8 in mid-term report.

*T 3.4 Ab initio DFT calculations for band alignments.* Investigation of band alignment by employing DFT calculations started in 2021 for MAPI – metal oxide interfaces were continued in 2022. Thus, interfaces between MAPI and several candidates for HTMs and ETMs, relevant for PSCs, have been investigated. Specifically, we considered the following interfaces: MAPI@$Cu_2O$, MAPI@NiO, MAPI@ $Cu_xNi_{1-x}O$ and MAPI@$SnO_2$. The influence of vacancies and interstitials was analyzed. Because NiO is anti-ferromagnetic, spin polarized calculations on a double supercell were performed in this case. The results are detailed in deliverable D4 in the mid-term review.

## WP4: Device characterization and modelling

*PP (NIMP), P3 (NIPNE) and P2(RU) had worked in this workpackage:*

**T 4.1** Photovoltaic characterization of standard and inverted PSC devices, by performing J-V scans to all the PSC devices were fabricated during 2022, employing for some representative samples also other type of investigations as EIS, EQE FTIR (**PP**).

**T 4.2** Development of the stochastic multi-scale m-DEM model, based on a new Ansatz for the recombination current ($J_{rec}$) and explains both, the apparent inductance and the large capacitance, providing the link to a microscopic description of these effects and a bridging point between the different approaches of known charge accumulation and charge collection models. (**P3, PP and P2**)

**T 4.3** Numerical analysis of bias stress tests, by characterizing and modelling the hysteretic behaviour of PSCs under different bias and light conditions (**PP, P3 and P2**)

## WP5: Device encapsulation and modules production and testing in standard operation conditions. Both PP(NIMP) and P4 (WATTROM) had jointly worked on:

**T 5.1** Encapsulation of the individual small and large area PSCs. Small and large area standard PSCs were fabricated by **PP** with *slot-die printing technique*, eliminating the toxic processing step of "solvent extraction". This healthy approach has an important drawback-the solvent used to prepare the "ink" remains partly in the deposited perovskite layers. In such situation the encapsulation procedure developed together with **P4** does protect against ambient factors (humidity, light, Oxygen) but cannot prevent the continuous slow degradation caused by the remaining solvent in the perovskite layer (intrinsic factor).

## WP6: Management, reporting, dissemination and patenting

**All the partners** participate in managing their resources and disseminate the results. **PP(NIMP)** took care of the project management, project webpage and made the yearly report based on the specific contributions of the partners.

---

Overview of the progress of work towards the objectives of the project, including milestones (M) and deliverables (D) identified in the project contract for year 2022.

---

- **D5 Report on deposition and characterisation of CuOx and Cu:NiOx layers in inverted PSCs.** A summary of the work performed in 2022 is given below.

The employed physico-chemical characterization techniques are:

(a) The surface and cross-sectional morphology of films deposited onto the mirror-polished Si <100> substrates was investigated by field emission scanning electron microscopy (FE-

SEM), using a Carl Zeiss Gemini 500 system. The micrographs were recorded under high vacuum (~3 – 7 × 10–5 Pa) at electron high tension voltages of 5 kV (top-SEM) and 10 kV (cross-SEM) and working distances in the range of 3.5 – 6.5 mm.

(b) The Ni/(Ni+Cu) concentrations and the chemical state of Cu and Ni were analysed by X-ray photoelectron spectroscopy (XPS), with the help of a SPECS system equipped with a Phoibos 150 mm hemispherical energy analyser with a multi-element two-stage transfer lens and a nine channeltron detector array. The XPS studies were performed using monochromatic Al Kα radiation (1486.7 eV) at a pressure of ~10–7 Pa and an X-ray source power of 300 W. A pass energy of 20 eV was used for the high-resolution core level spectra. The sample neutralization during the measurements was realised using a flood gun, at an acceleration energy of 1 eV and an emission current of 1 mA. The samples were analysed prior and after an in-situ Ar+ ions etching stage, performed for 5 min, at an energy of 3 keV and a pressure of ~1 × 10–3 Pa.

(c) The crystalline quality and phase composition of the films was investigated by X-ray diffraction in Bragg-Brentano mode, using a Rigaku SmartLab 3 kW system with CuKα radiation (λ = 1.5418 Å). The diffraction patterns were acquired in the angular range of 30–70° (2θ) with a step size of 0.02° and a scan speed of 0.75°/min.

(d) The chemical structure of the films deposited onto the IR transparent double-polished <100> Si substrates was studied by Fourier-transform infrared (FTIR) spectroscopy in transmission mode. The FTIR spectroscopy analyses were performed with a Jasco 6800-FV-BB spectrometer (Jasco Corporation, Tokyo, Japan) in the wave numbers range of 4000–100 cm–1, at a resolution of 4 cm–1, under vacuum.

(e) The optical properties of the films were investigated by conventional spectroscopy (transmission) using a Woollam Variable Angle Spectroscopic Ellipsometer equipment. The as-sputtered CuOx and Ni:CuOx film thicknesses were determined by spectroscopic ellipsometry (SE) using the same equipment, in the 1.2–4 eV spectral range, step of 0.01 eV, at three angles of incidence: 45°, 60° and 75°. A Cauchy dispersion was used to model the CuOx-based films.

(f) The electrical properties of the films were inferred by Hall measurements performed at RT using a system constituted of a Janis (SHI-4ST-1) cryostat, a LakeShore (EM4-HVA) electromagnet, a Lake-Shore (331S) temperature controller, a LakeShore (DSP 475) Gauss meter, a Keithley 2612A current/voltage source, a digital multimeter Agilent (34301A), and a Pfeiffer (HiCube80) vacuum system. The electrical contacts (wires) were soldered using indium in the corners of each squared specimen.

### 1) Cu and Ni oxides deposited and characterized by PP.

*1. Design of the HTM layer preparation experiments.* - the translation to large-area PSCs – efforts have been devoted by PP in 2022 to retrofit a new generation magnetron cathode (4-inches in diameter) to the existent RF-MS, aiming to improve the structural uniformity of the HTM layers on substrates of larger area. The retrofitting of the new cathode was successful, as demonstrated by XRD measurements in Fig.3, collected for films fabricated with the old and new magnetron cathodes. While in the case of the old cathode depositions, the films were majorly constituted of the lower-temperature Cu2O phase (ICDD: 01-073-6237), with the new cathode, the films were composed of the high-temperature CuO phase (ICDD: 00-041-0254). This is indicative of higher temperature radiative processes, determined by the stronger magnets of the new cathode, and subsequently more intense ion bombardment processes at the surface of the target (Figure 4).The implementation of the new cathode induced a radical improvement in the structural uniformity of the films.
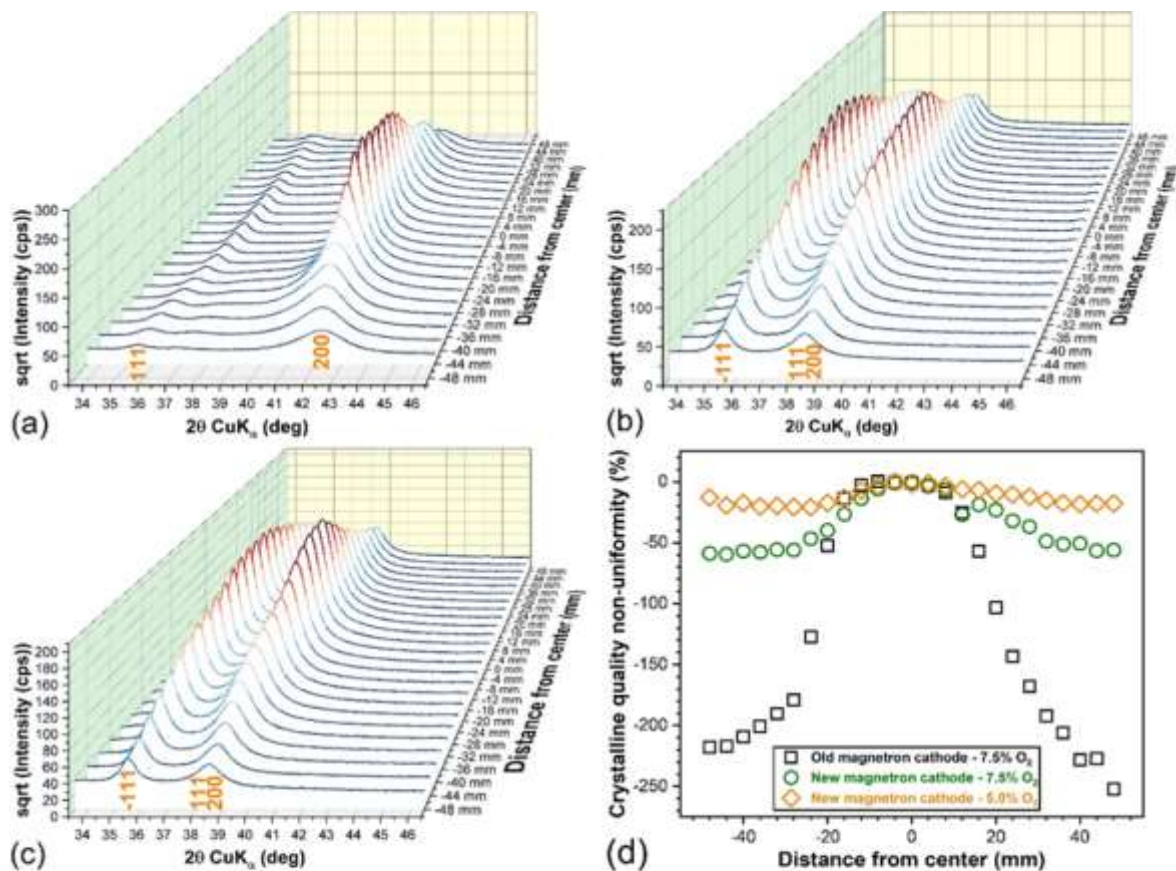
**Figure 3:** XRD mapping measurements collected along the diameter of the $CuO_x$ films deposited onto 4-inch Si wafers using the (**a**) old and (**b,c**) new magnetron cathode at a total working gas pressure of 0.3 Pa, target-to-substrate distance of 35 mm, and oxygen-to-argon dilutions of (**a,b**) 7.5% and (**c**) 5%. (**d**) Comparative crystalline quality non-uniformity profiles inferred for the samples analysed in (**a–c**) on the basis of the FWHM values extracted for the (**a**) 200 and (**b,c**) -111 peaks of the $Cu_2O$ and $CuO$ phases, respectively.
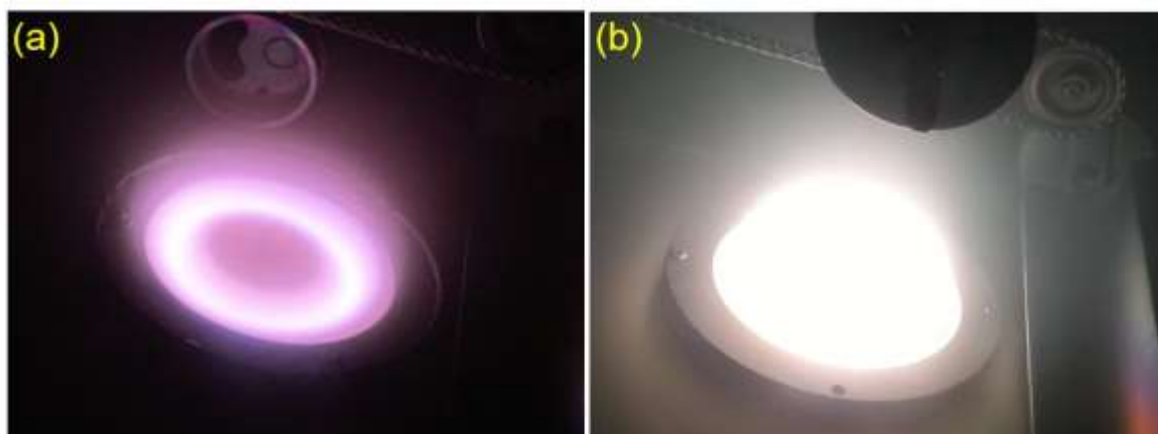


**Figure 4:** Plasma ignited by the (**a**) old and (**b**) new magnetron cathodes.

**Iceland**
**Liechtenstein**
**Norway** grants

ue FISCDI
Executive Agency for Higher
Education, Research, Development
and Innovation Funding

**2) Ni and Cu-doped Ni oxides deposited by P1 and characterized by both P1 and PP**.

In 2022 another set of films were deposited by P1 either by magnetron sputtering or electron beam evaporation on fused silica and *n*-type silicon substrates-see Table 2 below.

Table 2. Deposition parameters for NiOx and NiOx: Cu samples

| Nr. | Sample name | Substrate temperature (°C) | Sputtering Target/ *E beam conditions* | RF power (W) / *Base pressure (Torr)* |
|---|---|---|---|---|
| 1 | NiO | 150 | NiO | 70 |
| 2 | NiO:Cu-S1 | 150 | NiO:Cu | 70 |
| 3 | NiO:Cu-S8 | 150 | NiO/NiO:Cu | 50/70 |
| 4 | NiO:Cu-S14 | 150 | NiO/NiO:Cu | 40/70 |
| 5 | NiO: E beam –S1 | RT | *low oxygen partial pressure* | *1.1E-7* |
| 6 | NiO: Ebeam-S2 | RT | *high oxygen partial pressure* | *8E-8* |

The thickness of all the $NiO_x$ films were determined by spectroscopic ellipsometry to be ~15 nm. The optical transmittance of the $NiO_x$ films as well as the binding energies of Ni and Cu core levels in NiOx:Cu were determined by P1-UiO – examples given in Figs. 5 and 6.

For XRD measurements, NiO and NiO:Cu thin film of ~ 100 nm were deposited on silicon substrate.On this set of samples PP employed XRD analyses, shortly described here. The grazing incidence XRD measurements (Figure 7-a) indicated that, irrespective of composition, all films consisted of a cubic nickel oxide-type phase. The as-determined crystallite sizes are presented in Figure 7-b. Important differences in the crystalline quality of the films were noticed, with the underlying rationale being scheduled to be revealed, following by a series of in-depth investigations, in the next stage of the project.
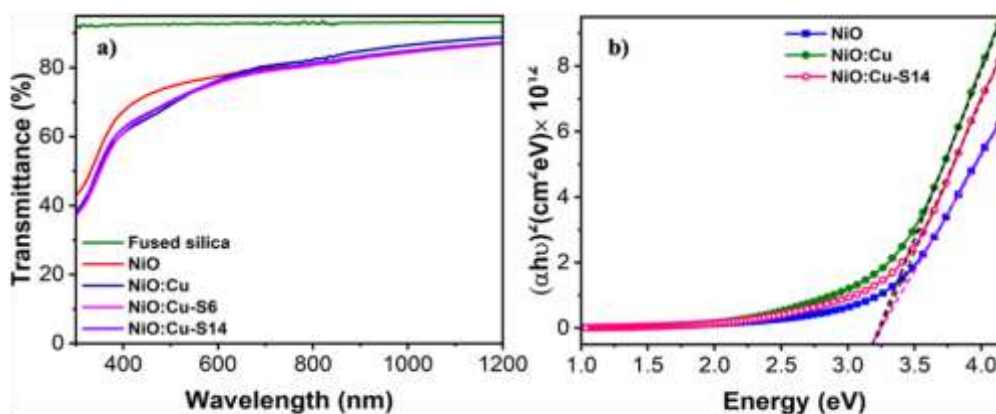


**Figure 5.** (a) Transmittance of the 15 nm $NiO_x$ and NiOx:Cu thin film. (b) Tauc plot for $NiO_x$ and NiOx:Cu samples.

Iceland
Liechtenstein
Norway grants

ue fiscdi
Executive Agency for Higher
Education, Research, Development
and Innovation Funding
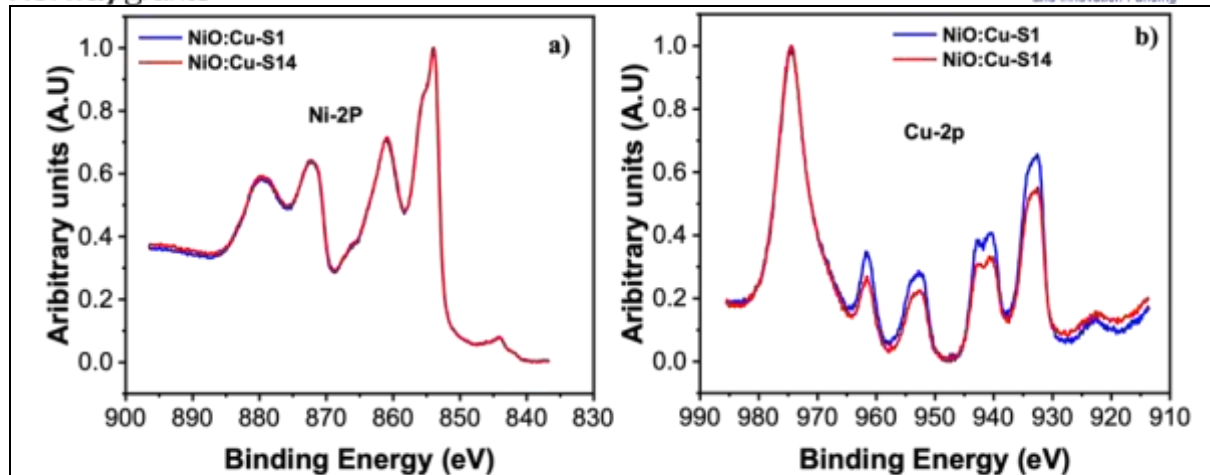
**Figure 6.** (a) XPS data of Ni core level of $NiO_x$ and NiOx:Cu thin film. (b) XPS data of Cu core level of NiOx:Cu thin film
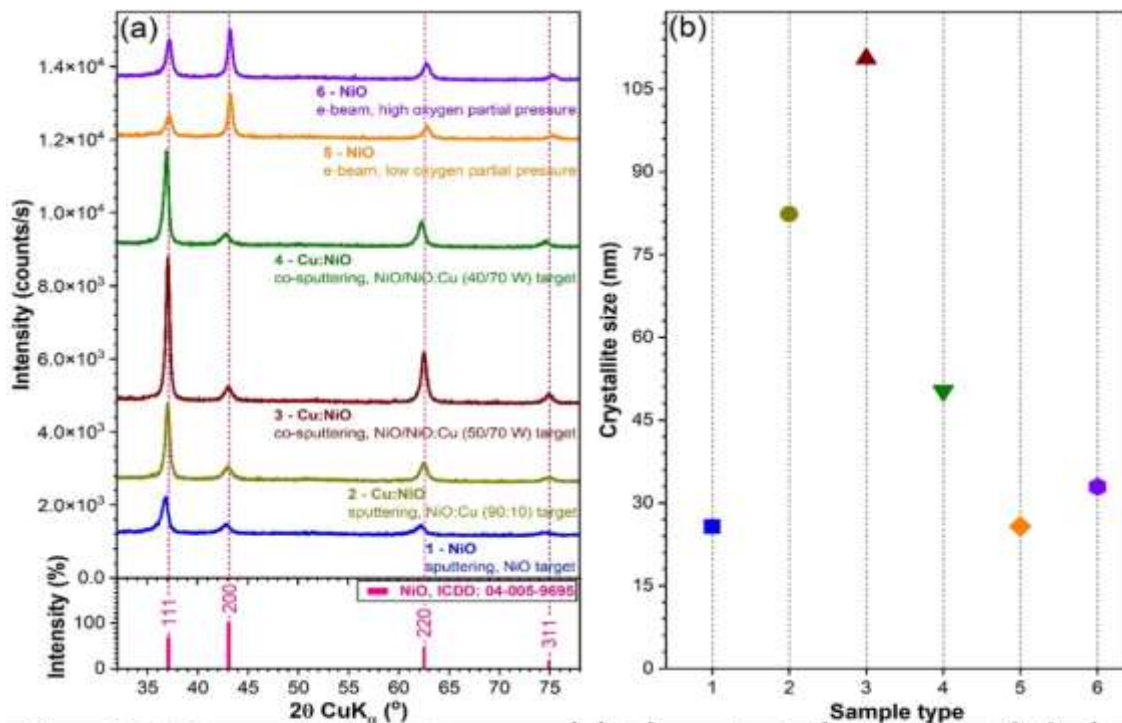


**Figure 7:** (a) Comparative XRD patterns, recorded in the grazing incidence mode (α=2°), for the thin (~100 nm) $NiO_x$ (samples 1, 5, and 6) and Cu:$NiO_x$ (samples 2, 3, and 4) films. At the bottom of (a) frame is presented (as sticks) the ICDD reference diffraction file of cubic NiO (ICDD: 04-005-9695) phase. (b) Crystallite sizes determined at the (111) crystal plane by applying the Scherrer equation.

- *D6 - Stochastic multi-scale m-DEM model & D9- Numerical analysis of bias stress tests*

In phase II of the project, a dynamic electrical model has been developed which describes the main features of the dynamic J-V charateristics and of the small signal analysis. The large signal analysis comprises J-V simulations performed with different voltage poling (bias stress) and illumination conditions, while the influence of the scan rate and characteristic time scales on the hysteresis magnitude is shown. At top level the model is based on an equivalent circuit, which includes the standard elements of a solar cell and a sub-circuit describing the recombination current based on ionic charge accumulations and ionic currents - Fig. 8. The circuit elements are in direct correspondence with the building-blocks of the PSC (e.g. absorber ionic resistance, capcitences of the interfaces between the perovskite and HTL, HTM layers) and processes (e.g ion migration, recombination current).

Specific information about the behavior of a given element can be plugged-in from a microscopic description (e.g. molecular dynamics simulations of ion migration performed by LAMMPS). Thus, we successfully introduced a comprehensive equivalent circuit model, able to reproduce both capacitive and inductive effects, which can include microscopic descriptions of the underlying elements.
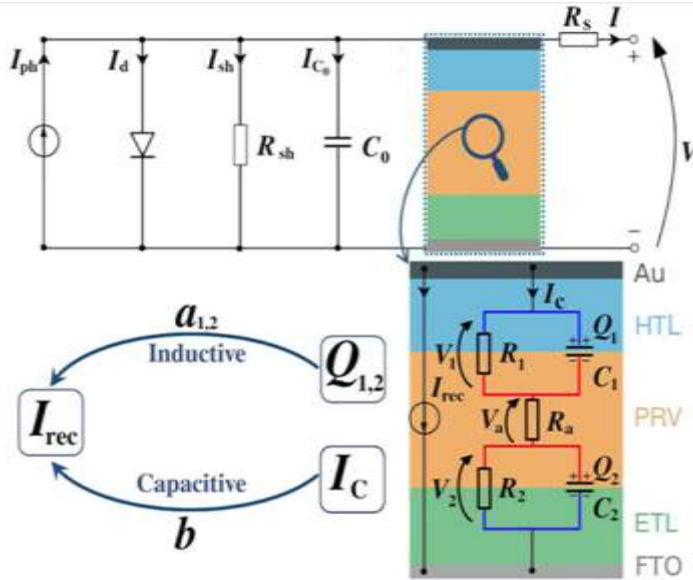


**Figure 8:** *The equivalent circuit model employed for describing capacitive and inductive effects. The colorful sections represent the PSC elements in standard configuration with FTO and gold electrodes.*

The backbone of our circuit model is composed from standard elements such as the current source corresponding to the photogenerated current $I_{ph}$, the diode element introducing a recombination current $I_d$, the shunt resistance $R_{sh}$, accounting for a recombination current $I_{sh}$, and the series resistance $R_s$ plus a small geometrical capacitance $C_0$, counting for the hysteretic effects. And we have also introduced the two essential parts, namely the R-C circuit block and the additional current source corresponding to the ionic modulated recombination current, Irec. The two parallel groups, $R_1$-$C_1$ and $R_2$-$C_2$ (R-C circuit) are in series with the perovskite absorber ionic resistance Ra. The corresponding charges ($Q_1$ and $Q_2$) for the capacitors $C_1$ and $C_2$, with instantaneous applied voltages $V_1(t)$ and $V_2(t)$, describe the ionic charge accumulation at the tow interfaces, between the absorber and the hole transporter layer (HTL) and the electron transporter layer (ETL). While, $R_1$ and $R_2$ resistances account for the electron or hole-ion charge neutralization at the two interfaces and can be regarded as loss resistances for the ionic capacitors. In this picture, the current $I_c$ denotes the ionic current flowing inside the perovskite absorber layer. The precise values and, potentially, the voltage dependence of ionic resistance and ionic capacitances can be extracted from molecular dynamic simulations performed by RU partner, using the LAMMPS code, which describes the ion/vacancy drift and diffusion in the absorber layer. Thus, a microscopic description based on atomistic simulations can provide an important input for the equivalent circuit model. The dynamic J-V characteristics is obtained from the coupled systems of differential equations:

$$\frac{\partial V_1}{\partial t} = -\frac{1}{C_1}\left(\frac{R_a + R_1}{R_a R_1}\right)V_1 + \frac{V + IR_s - V_2}{R_a C_1},$$

$$\frac{\partial V_2}{\partial t} = -\frac{1}{C_2}\left(\frac{R_a + R_2}{R_a R_2}\right)V_2 + \frac{V + IR_s - V_1}{R_a C_2},$$

$$I_{ph} - I_d - I_{sh} - I_{c0} - I_c - I_{rec} - I = 0,$$

**Eqs. (1-3):** *The equations governing the large-signal behavior in the dynamic regime.*

Since the essential contribution to the hysteretic effects in the J-V characteristics and the capacitive and inductive effects comes from the recombination current $I_{rec}$, we have based the model on the central assumption that the recombination current $I_{rec}$ is modulated by both ion charge accumulation and ionic current, using the following Ansatz:

$$I_{\text{rec}} = I_{\text{rec0}} + \sum_{i=1}^{2} a_i Q_i + b I_c,$$

**Eq. (4):** *The recombination current depends on the ionic charge and ionic current.*

We have used the term, $I_{rec0}$, as the reference recombination current, in the absence of the ionic influence, which simply regauges the photogenerated current, while $a_i$ and $b$ parameterize the inductive and capacitive recombination current contributions.

  For the reference PSC we assign a set of equivalent circuit parameters as the: series resistance $R_s$ = 50 Ω; shunt resistance $R_{sh}$ = 6 k Ω; photogenerated current $I_{ph}$ = 2 mA; diode parameters $I_s$ = 10−13 A and $n_{id}k_BT$ = 40 meV; geometrical capacitance $C_0$ = 0.079 µF; PSC area $A$ = 0.09 cm$^{-2}$; absorber (ionic) resistance $R_a$ = 500 k Ω; ionic capacitor parametrization (one capacitor case) $^-C_{01}$ = 10 µF, $^-C_{11}$ = 10$^{-14}$ µF, $n_c k_B T$ = 26 meV. In this initial PSC configuration only, the capacitive effects are accounted for ($a_i$ = 0, $b$ = 1000), while the ionic capacitor losses are initially neglected ($R_{1,2} \rightarrow \infty$). The parametrization of $I_{rec}$ as a function of $I_{ph}$ is given by $\lambda_0$ = 0.5, $\lambda_{a0i}$ = 10 s$^{-1}$, $\lambda_{ai}$ = 50 mC$^{-1}$, $\lambda_b$ = 500 mA$^{-1}$.

The small signal analysis reveals the capacitive and inductive effects, which are here identified to follow from two distinct recombination processes, namely the action of the bulk electric field and ionic-induced defect recombination. Starting with the large signal equivalent circuit shown in Fig. 8 and applying the following three equations, we obtained the small signal circuit, by excluding the constant current source element ($I_{ph}$) and replacing the diode element with dynamic resistance $R_d = n k_B T/(q_e I_d)$. Dynamic hysteresis effects presented by the J-V scans hints to underline the capacitive effects. The physical capacitances identified as an ionic capacitance, while the apparent capacitance extracted by electrochemical impedance spectroscopy (EIS) is significantly larger under illumination and it is due to a modulation of the collected current or, equivalently, the recombination current, driven by the instantaneous electric field produced by the ion distribution. In the following we describe the analyzed capacitive and inductive effects.

**1.Capacitive effects**
     The modulated recombination currents may be one key aspect for the significant enhancement of the apparent capacitance $C_{app}$ when increasing the illumination. We start our analyze by neglecting the inductive effects and we set in Eq 1 the parameter $a$ = 0, this way, in the simulated EIS the $b \times I_c$ term controls the recombination current. Figure 9 presents the Nyquist plot analysis and the frequency dependence of $C_{app}$, starting with practically dark conditions ($I_{ph}$ = 2 × 10−3 mA) and up to the maximum considered illumination intensity ($I_{ph}$ = 2 mA).
Considering the working point $V_{wp}$ = 0.7 V, close to the maximum PCE point, with the PSC in the stationary regime. Under dark conditions, two plateaus can be identified, one corresponding to the ionic capacitance ($C_{ion} \approx 10$ µF) and the other one corresponding to the geometrical capacitance ($C_0 \approx 0.07$ µF). These results are consistent with various EIS measurements and experimental data. Correspondingly, the Nyquist plot shows two arcs, one belonging to the ionic capacitance at low frequencies and one to the geometrical capacitance at high frequencies.
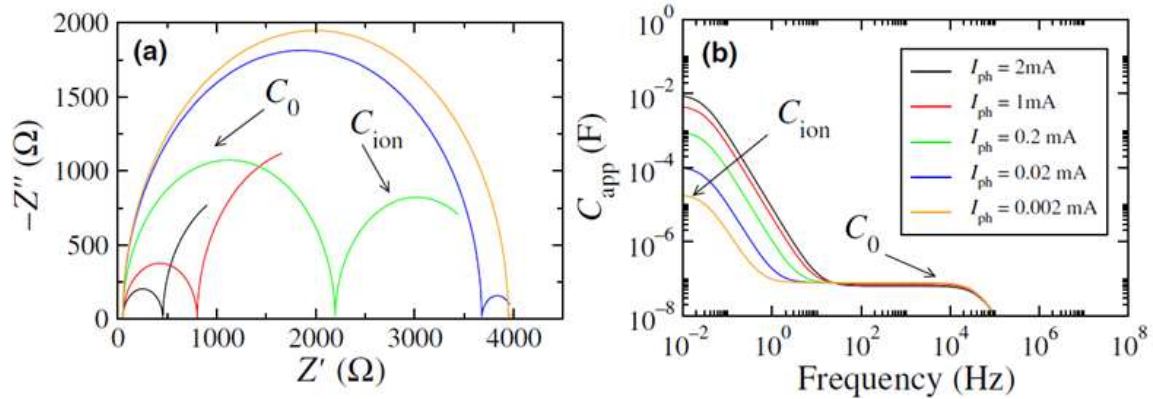
**Figure 9:** *Capacitive effects evidenced by EIS analysis, for several illumination intensities, set by the photogenerated current Iph = 2, 1, 0.2, 0.02, 0.002 mA: (a) Nyquist plot and (b) the apparent capacitance (Capp) as a function of frequency. Under practically dark conditions ($I_{ph}$ = 0.002 mA) the ionic capacitance ($C_{ion}$) is found at low frequencies, while at higher frequencies the geometrical capacitance ($C_0$) is evidenced. However, $C_{ap}$p increases sharply with illumination intensity, as in typical EIS experiments.*

## 2. Inductive effects

In some PSCs the inductive effects may appear at small or intermediate frequencies. So, here we argue that the inductive behavior can be produced by defect induced recombination controlled by ionic accumulations at the interfaces, which is introduced by the term $a \times Q_C$. Figure 10 presents the changes in the Nyquist plot and $C_{app}$ -f dependence for $a$ = 0, 5, 10, 30, 40 s−1.
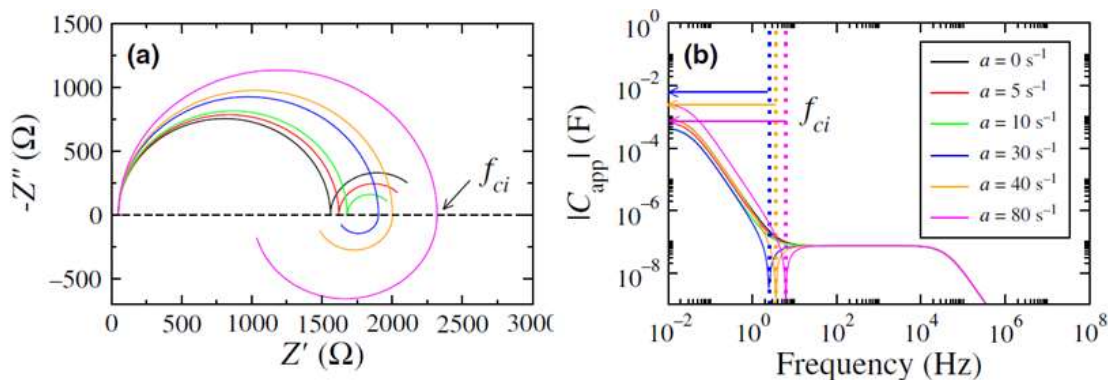


**Figure 10:** *Inductive behavior produced by ion-defect-induced recombination. By increasing the parameter a in the sequence 0, 5, 10, 30, 40, 80 s−1, the recombination current is enhanced leading to significant inductive effects. These are visible in the Nyquist plot (a) and they correspond to the frequency ranges marked by arrows (b). The threshold frequency fci marks the transition between the capacitive and inductive behavior.*

Smaller values of *a* still produce a capacitive behavior, while larger ones make the inductive effect visible at low frequencies, eventually overcoming the intrinsic capacitive behavior. To capture the sign change of *Im[Z]*, we consider in this case a lower value for the parameter that controls the capacitive behavior by the electric field induced recombination, $b$ = 100. In a similar manner with the huge apparent capacitances observed under illumination, we observe relatively large inductances in the EIS experiments, both having their origin in a modulated recombination current, which grows significantly with the illumination. However, the inductive effects can be related to the ionic-induced defects, mostly located at the interfaces, as opposed to the capacitive effects that are due to the instantaneous electric field in the bulk of the perovskite. The ion mobility, as well as the susceptibility to induce defects, is an important prerequisite for the inductive behavior.

Therefore, the inductive effects may be regarded as a quantifiable feature for defect analysis and recovery in monitoring the PSC degradation. There is also a clear dependence between the inductive behavior and the working point used in the EIS measurements, as presented in the figure 11.
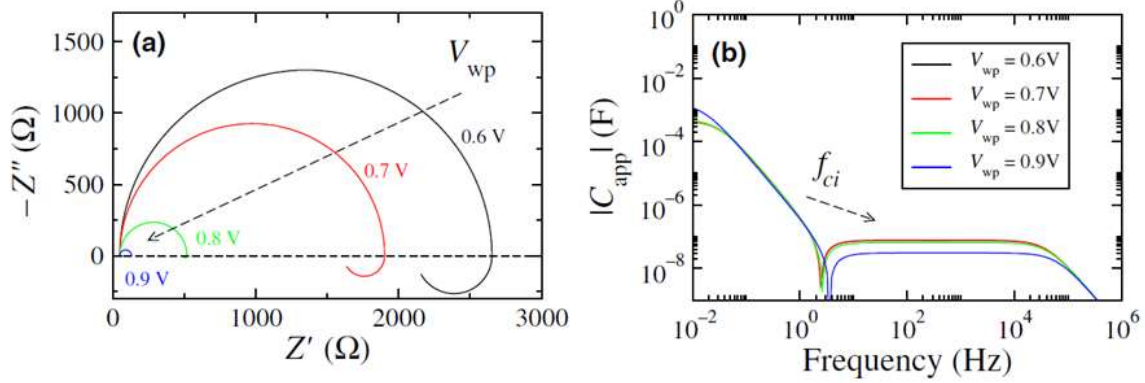


**Figure 11:** *Working point ($V_{wp}$) influence on inductive behavior for a = 30 s⁻¹ (a) Nyquist plot showing an enhancement in the sample conductivity. (b) The absolute value of the $C_{app}$, indicating an increase of threshold frequency ($f_{ci}$) with $V_{wp}$, where the capacitive effect is switched into an inductive one and, also, a small increase in the apparent inductive effect by increasing $V_{wp}$ at low frequencies.*

The magnitude of the inductive effects increases at larger $V_{wp}$ and low frequencies, due to larger ion accumulations. Furthermore, the transition point between the capacitive and inductive behavior, marked by $f_{ci}$, drifts towards higher frequencies. The shift of $f_{ci}$ with increasing $V_{wp}$ induces an interesting conversion from a capacitor to an inductor which may also support the idea that large ionic accumulations at positive voltages may induce the type of recombination that is responsible for inductive effects. The phasor diagrams shown in Figure 12are a perfect representation of the capacitive and inductive behavior for the current components in the small signal analysis regime. When applying a small signal with amplitude $v_0$ = 1 mV, the measured current i is dephased by the two different recombination mechanisms. The parallel impedances $Z_L^{eq}$ and $Z_C^{eq}$ have the decisive contributions for this dephasing, where the small signal recombination currents $I^L_{rec}$ and $I^c_{rec}$ are found from v + iRs = $I^L_{rec} Z_L^{eq}$= $I^c_{rec}$, $Z_C^{eq}$. The currents $I^L_{rec}$ and $I^c_{rec}$ are dephased by π/2, as the former is proportional to $Q_c$ and the latter with $\partial Q_c/\partial t$. It is worth noting that there is a connection between capacitive and inductive effects, as the former depends on the ionic current, $\partial Q_c/\partial t$, while the latter is connected to the ionic charge accumulations, $Q_c$. The recombination current is, in general, a sum of these two components and the parameters ***a*** and ***b***, which are sample specific, will establish one of the two behaviors.

   In addition to the low-frequency inductive behavior, for some PSCs we see two or three arcs in the Nyquist plot, which is indicative of multiple relaxation-time scales relevant for the capacitive behavior. The rather different time scales may originate from the migration of several ionic species (iodine, methylammonium ions, their charged vacancies) and/or their accumulation at both interfaces. The capacitances associated with the two interfaces can be rather different taking into account the ionic diffusivity at the ETL-perovskite and HTL-perovskite interfaces and the ion distribution.

In Figure 13 we see the case with two ionic species (the negative iodine ions and the positive iodine vacancies) migrating towards both interfaces, with different time scales. The two capacitors are parametrized by⁻ $C_{01}$ = 20 μF, ⁻$C_{11}$ = 2 × 10⁻14 μF, ⁻$C_{02}$ = 1 μF, ⁻$C_{12}$ =10⁻15 μF, $n_c k_B T$ = 26 meV, i.e., we have $C_1/C_2$ = 20. In this case, the $Q_1$ is most significant and it generates the inductive effect at low frequencies, while $Q_2$ produces negligible inductive effects. The two capacitive arcs in the Nyquist plot correspond to $C_0$ and $C_2$. However, if $a_2$ >> $a_1$, i.e., the second interface has a larger impact on the recombination current.
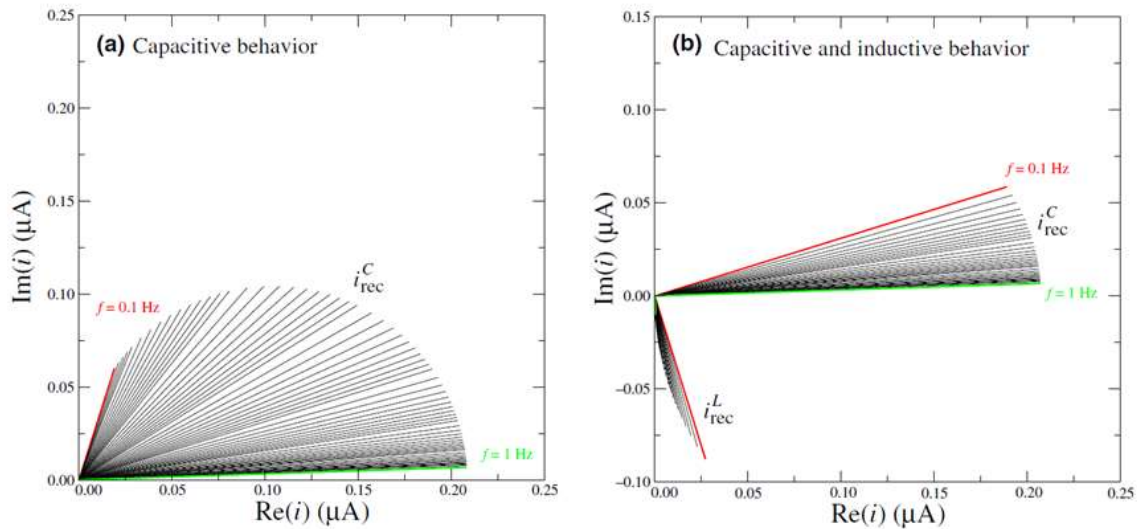
**Figure 12:** *Phasor diagrams showing the dephasing of the recombination currents in the range of frequencies f = 0.1–1 Hz for two types of PSCs, with: (a) capacitive effects only (a = 0, b = 100) and (b) capacitive and inductive effects (a = 30 s−1, b = 100). The diagrams correspond to the data sets shown in Fig. 5. The small signal voltage v(t = 0) has zero phase, i.e., it is oriented along the x axis (i = 0). In subplot (b) the π/2 dephasing between $I^c_{rec}$ and $I^L_{rec}$ is evidenced.*
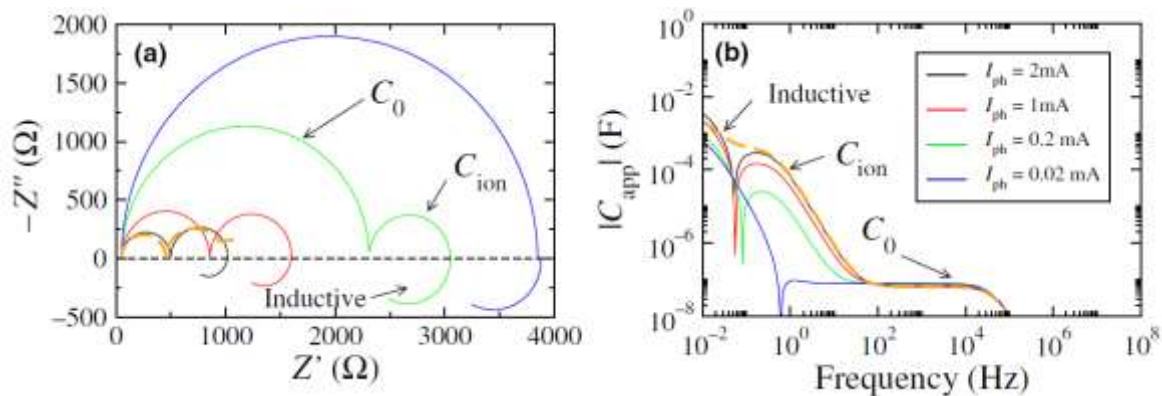


**Figure 13:** *Two active interfaces with inductive effects: (a) Nyquist plot and (b) $C_{app}$-f plot. Three different illuminations ($I_{ph}$ = 0.2, 1, 2 mA) are considered.*

The interfaces have different capacitances with the ratio $C_1/C_2 = 20$. Therefore, we identify the second semicircle $C_{ion}$ to $C_2$ capacitance, while the arc corresponding to $C_1$ turns into the negative (inductive) region. The dashed lines correspond to the vanishing inductive contribution for $I_{ph} = 2$ mA. While the large signal analysis based on dynamic J-V characteristics has been investigated in numerous studies and detailed features of the hysteric effects have been linked to specific measurement conditions, the intriguing capacitive effects were highly debated, while the inductive behavior remains rather elusive. In the following, we present a selection of the most representative types of EIS measurements. The investigated PSC samples have a standard configuration consisting of planar layers as follows: glass substrate coated with fluorine-doped tin oxide (FTO), compact

and mesoporous TiO2 layers deposited by spray coating, $CH_3NH_3PbI_{2.6}Cl_{0.4}$ mixed halide perovskite and spiro-OMeTAD deposited by spin coating and a sputtered Au top contact. Electrochemical impedance spectroscopy (EIS) responses of the fabricated solar cells were measured with a broadband dielectric spectrometer model Alpha-A High Performance Frequency Analyzer from Novocontrol (Montabaur, Germany). The EIS experiments were performed in ambient laboratory conditions, using an alternating current (a.c.) potential of 10 mV amplitude, frequencies in the $10^{-1}$ Hz − $10^7$ Hz range, d.c. potentials between -1 V and + 1 V and different illumination conditions given by a solar simulator, with the incident power varying between 0 and 100 mW/cm$^2$. A mask was used to ensure that only the active area of 0.09 cm$^2$ of the device was illuminated during the EIS measurements. The Ansatz concerning the exponential behavior of the capacitance as a function of applied voltage, in dark or under illumination, was confirmed experimentally.
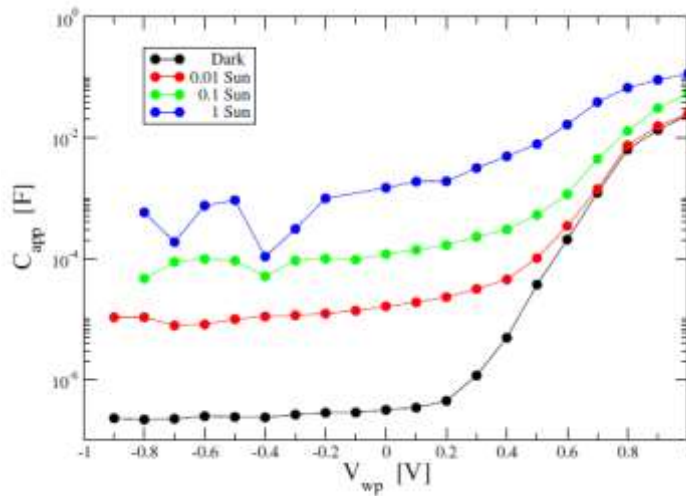


*FIG. 14. Experimental C-V data showing exponentially sharp increases at positive voltages. The same behavior is found for increasing the illumination intensity, while the capacitance plateau shifts towards higher values.*

The data shown in Fig. 14 was collected for a frequency f =100 Hz and different illumination intensities, although it is worth mentioning that a similar behavior is found for a wide range of frequencies (1 Hz - 1 MHz range). This is in close connection with a well known feature in the J-V hysteresis under pre-poling conditions with V > Voc – the current bump in the reverse characteristics, which is a direct consequence of the sharp increase of the capacitance close to Voc. A mere constant capacitor would not produce this effect, although a rather flat J-V hysteresis would still be obtained for sufficiently large capacitances. Important insights can be drawn from analyzing the capacitive and the inductive behavior under illumination. Fig. 15 showing the apparent capacitance-frequency dependence is illustrative to this end.
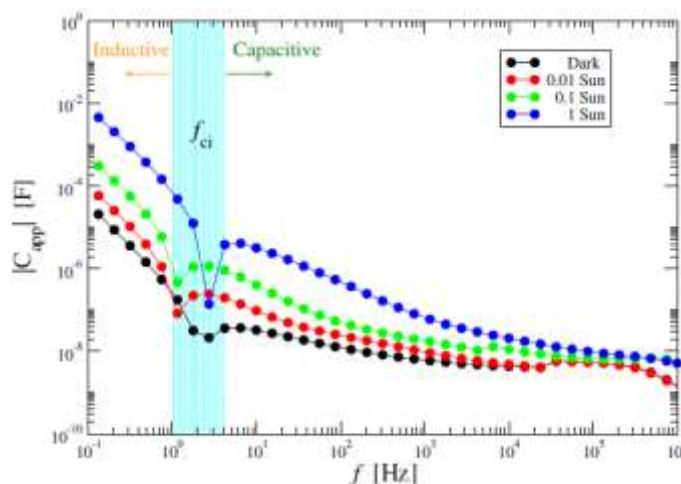


***Figure 15.*** *Measured C-f dependence obtained from analysis of EIS, for several light intensities and working point of 0.5 V. Inductive behavior is found in the lower frequency range, with a significant increase with light intensity, indicating the role of recombination currents of photogenerated carriers. The transition frequencies, $f_{ci}$, are located in a narrow frequency range marked by the colored rectangle.*

In dark conditions, the apparent capacitive and inductive effects (negative capacitances) reach moderate values ($10^{-5}$ −$10^{-4}$ F), as a consequence of ionic response and limited recombination. As the illumination is increased up to 1 sun, significant apparent capacitances and inductances emerge, which emphasizes the role of the recombination of photogenerated carriers. For capacitive behaviors this light-induced enhancement is rather well documented, in contrast to a similar trend for inductive effects under illumination.
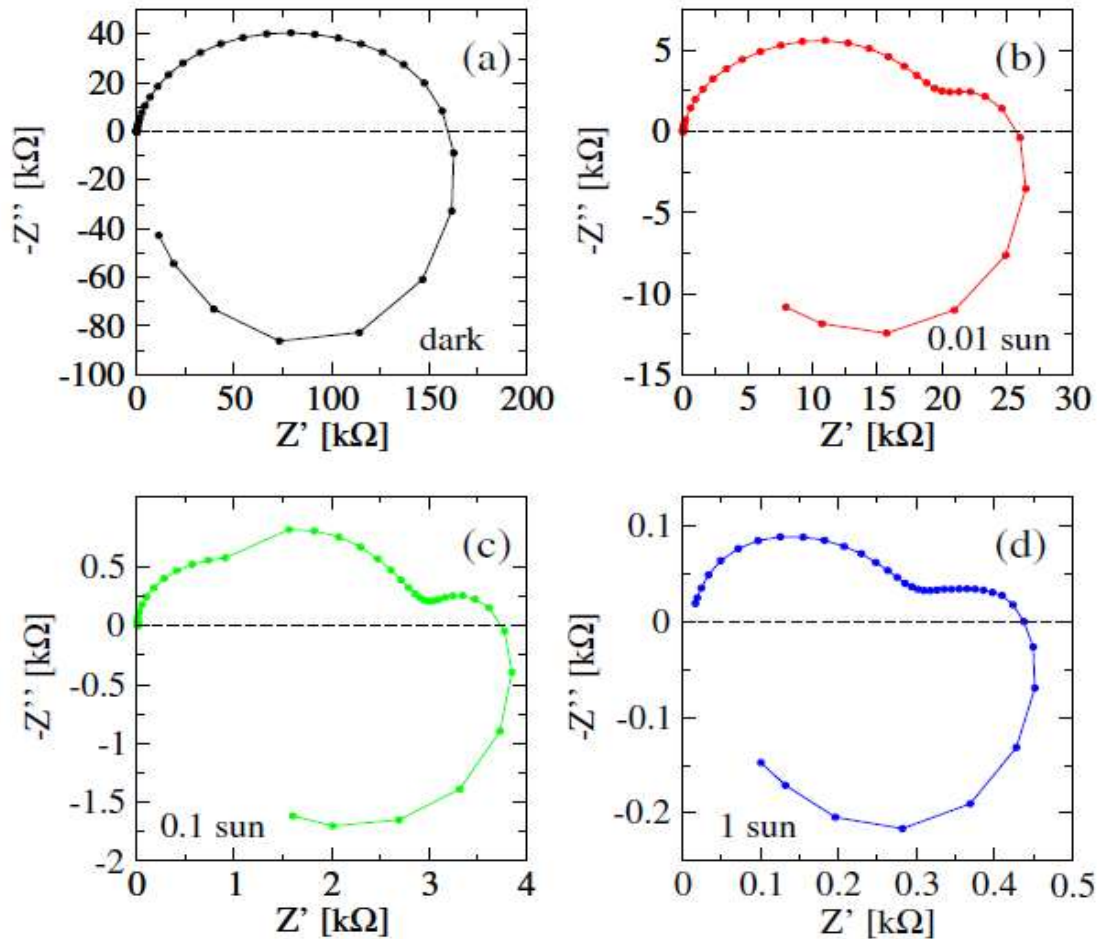


***Figure 16***. *Nyquist plots obtained from EIS measurements, obtained for a working point $V_{wp}$ = 0.5 V, under different illumination conditions: (a) dark, (b) 0.01 sun, (c) 0.1 sun and (d) 1 sun. Two capacitive semi-circles and an inductive behavior at low frequencies are evidenced.*

Typical Nyquist plots are shown in Fig. 16, which indicates the impedance reduction with illumination. Furthermore, Fig. 17 shows the modifications in the apparent capacitive/inductive behaviors as the working point, $V_{wp}$, is changed from 0.6 to 0.9 V.

The transition point ($f_{ci}$) shifts to higher values as $V_{wp}$ is increased, while the inductances are enhanced by approximately one order of magnitude. These observations are consistent with our simulations. Overall, the EIS experimental data supports the idea of ion-induced recombination of photogenerated carriers, as the magnitude of both capacitive and inductive effects is in strict correlation with the illumination intensity.
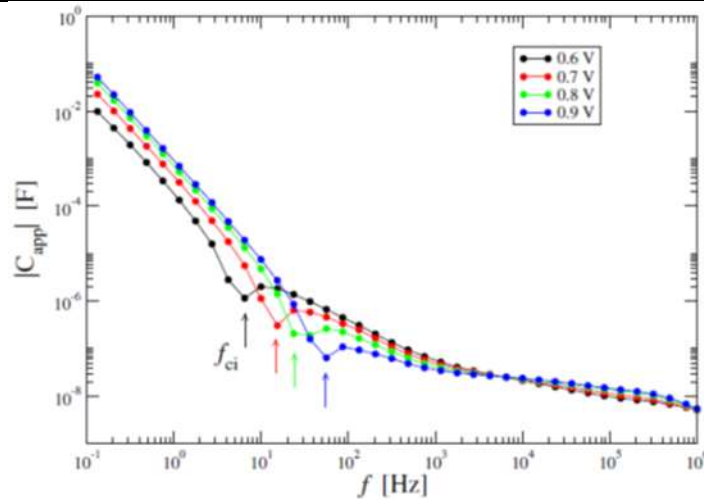
*Figure 17.* Experimental C-f data showing the shift of the transition frequency, fci, with the applied working point, $V_{wp}$ = 0.6, 0.7, 0.8, 0.9 V, while there is also a small increase of the inductive effects in the low frequency range.

In conclusion, we successfully introduced a comprehensive equivalent circuit model, able to reproduce both capacitive and inductive effects, which can include microscopic descriptions of the underlying elements. It recovers the known dynamical effects experimentally observed, such as the current bump in the reverse scan under positive poling, inverted hysteresis under negative poling, and tuning of the hysteretic effects under illumination and bias scan rate, correlated with the relatively large time scales involved in the ion migration processes. Our analysis provides a bridging point between the charge accumulation models and charge collection models. We show that both models can lead to similar results, being formally equivalent, provided that the time scale of the slow process is the same. Using the ansatz that one contribution to the recombination current comes from the ionic charge accumulations, we associated, in the CC model, the inductance to a de-phased recombination current. In the small signal analysis we see a clear identification of the contributions to the recombination current (associated with capacitive and inductive effects): the ionic current is linked to the electric field in the perovskite absorber, which, in turn, controls the electron-hole recombination, while the ionic charge accumulations at the interface determine the amount of defects modulating the recombination current. In our opinion, by monitoring the capacitive and inductive effects over time, which are related to ionic processes, one can predict long-term degradation of the PSC. Such studies will be further performed.

- ***D7 Report on deposition of compositional engineered perovskite layers by eliminating solvent extraction***

-

One of the project objectives is to avoid the anti-solvent used in the fabrication process of PSC structures. For achieving this objective, multiple working directions were undertaken during this project, one of these being represented by the <u>deposition for the perovskite layer using **slot die printing method** on large area substrates without using the solvent extraction technique</u>. Several studies were performed, varying different working conditions, in order to obtain stable perovskite solar cells with good PCE values. The results obtained until now are encouraging and PSC in standard configuration of around 8% were already reached in our group (see Fig. 18).
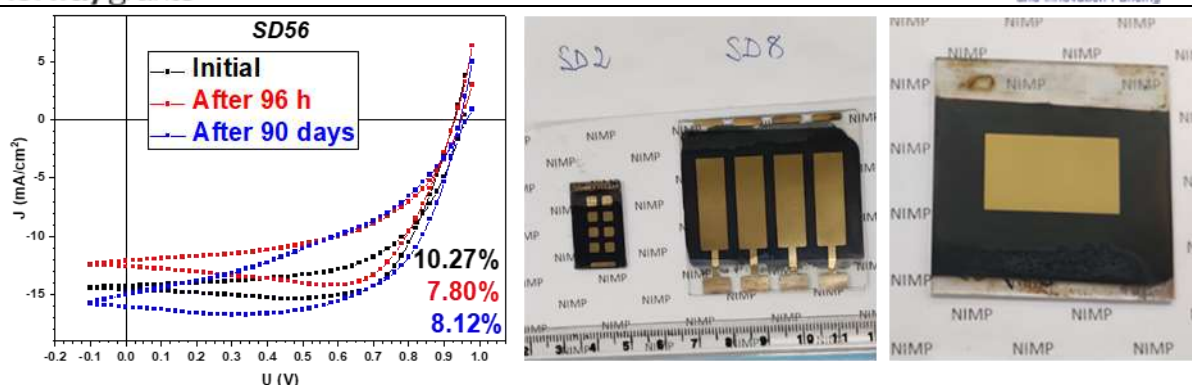
**Figure 18.** *Photovoltaic parameters and images of the obtained standard PSCs*

With respect to milestones **MS2&MS3 (Production of small and large area _standard_ PCS with stabilized PCE of minimum 20 % and 15% respectively)** we did not succeed yet to achieve such stabilized high values of PCE in PSCs deposited by large area techniques (slot-die). We still work on improving both PCE and performance stability.

For inverted PSCs we did not obtained encouraging results, especially due to the difficulties of depositing the PCBM layer. Thus, with respect to milestone **MS4 (Production of inverted PCS with PCE of minimum 15 %)** we are really far from achieving such stabilized high values of PCE in PSCs deposited by large area techniques (slot-die), especially due to difficulties and the random poor success in depositing the PCMB layer. We will continue working on inverted PSCs **only** if a low temperature deposition of Cu doped $NiO_x$ or Ni doped $CuO_x$ n-type films will be successful.

- ### D8    Map of electrostatic potential and impact of H2O molecules on perovskite stability

   Due to the large size of our system, the system had to be split up into several "chunks". This was done by taking the relaxed system data and finding the origin of the cell in the x, y, and z directions. From this, we extracted a single slice of the cell where the defect will then be placed using the LAMMPS code command compute chunk. The first defect introduced into the material was the interstitial iodide. We produced a potential energy map at the locations of all atoms held in the specific slice. A full video for a time interval of 0.5 ns can be seen here. We also recreated the study outlined above with a missing iodine. We created a video of a 0.5 ns time interval, that allows us to follow the movement of the vacancy throughout the system over time. We considered the interface of MAPI with $Cu_2O$ and NiO materials, and we included water molecules. The intention is to observe their effect of their electric dipole on the band alignment. In the following examples, three $H_2O$ molecules are included randomly on the MAPI side, near the interface. The figures 19 and 20 show the valence charge density and total electrostatic potential calculated for the x-z plane.



**Figure 19.** *The valence charge map at the interface MAPI@$Cu_2O$ in the x-z plane, averaged in the y-direction: (a) for the pristine system and (b) for the system with three water molecules in MAPI. The difference map is represented in (c). The arrows mark the region where the water molecules are located (at the interface in the perovskite).*
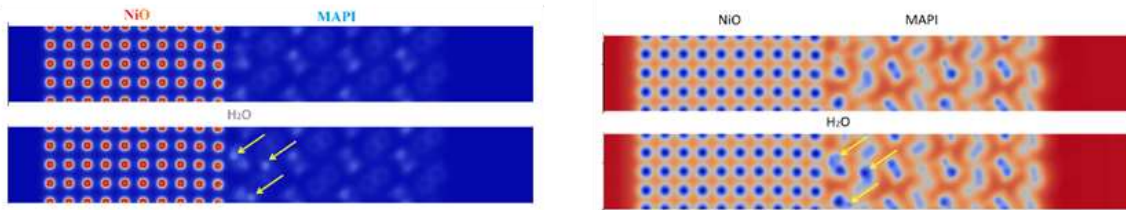
**Figure 20.** *The total electrostatic potential map at the interface MAPI@NiO in the x-z plane, averaged in the y-direction: (a) for the pristine system and (b) for the system with three water molecules in MAPI. The difference map is represented in (c). The arrows mark the region where the water molecules are located (at the interface in the perovskite).*

Similar maps are obtained for the z-y direction. The partial density of states (PDOS) analysis shows the influence of the water molecules on the electronic structure. In all cases, additional states appear in the proximity of the band gap, which has a detrimental impact on the charge separation.

- ### *D10    Report on encapsulation procedure& MS7 -Encapsulated individual small and large area PSCs*

Tests for encapsulation were performed with the same encapsulation foils used in the case of Si-based photovoltaic panels: EVA (ethylene-vinyl acetate copolymer) and PET (Polyethylene terephthalate Solar Backsheet). The encapsulation of silicon-based panels is typically made at 200 °C, but the PSCs does not resist to such temperatures. We found that a successfully bond can be achieved at temperatures of 80 °C. We present below some representative results obtained on small and large area PSCs fabricated by employing two different deposition methods:

a) perovskite solar cell fabricated by spin-coating technique *with solvent extraction step*
Figure 21 shows the photocurrent vs. applied voltage measured under 1 SUN illumination before and after encapsulation at 80 °C with EVA/PET foils. The encapsulated cell showed a good resistance to high humidity levels, up to 90%. Therefore, one can conclude that the developed encapsulation procedure is successful and can be safely applied.
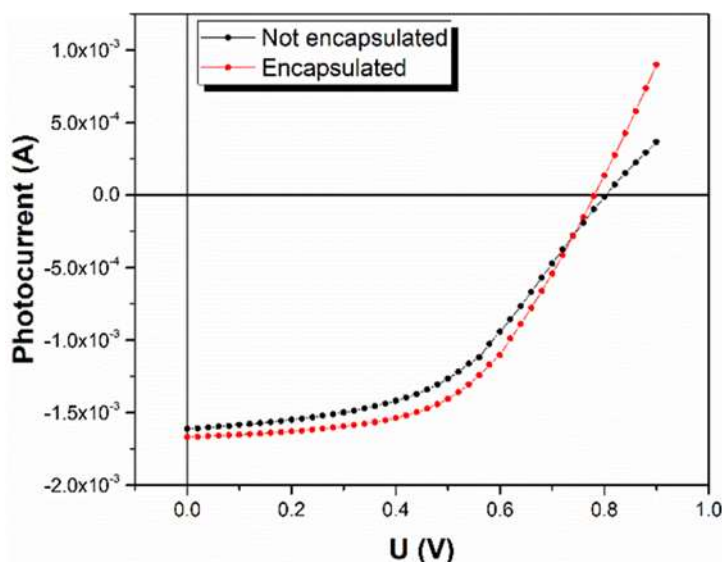


**Figure 21:** *Photocurrent vs. voltage curves for solar cell under 1 SUN AM 1.5 irradiation; before (black) and after (red) encapsulation.*

b) perovskite deposited by slot-die technique without the use of the antisolvent step
In this case the thermal treatment at 80° C needed for curing the EVA and PET encapsulating foils leads to a significant decrease in PCE (up to 25% decrease). The experiments with varying the curing temperature show that the PCE degradation in time is similar for both non-encapsulated and encapsulated cells indicating an internal degradation mechanism, independent of external factors like humidity. Following the diverse employed

investigations (described in detail in mid-term report at MS7) our conclusion is that part of the solvent used for the deposition of the perovskite layer is still embedded in the priscine perovskite layer and it slowly degrade the perovskite chemical bonds. Thus, further studies and developments are needed to find the proper technology for eliminating the solvent without using a toxic anti-solvent.

Photos of small and large area encapsulated PSCs are given in Fig. 22.

*With respect to MS7, we concluded that the developed encapsulation procedure can be successful applied on small and large area PSCs, fully protecting the PSCs against external ambient factors.* The degradation observed on PSCs deposited by slot-die printing technique is not caused by the encapsulation procedure but by intrinsic material factors on which we will focus further.
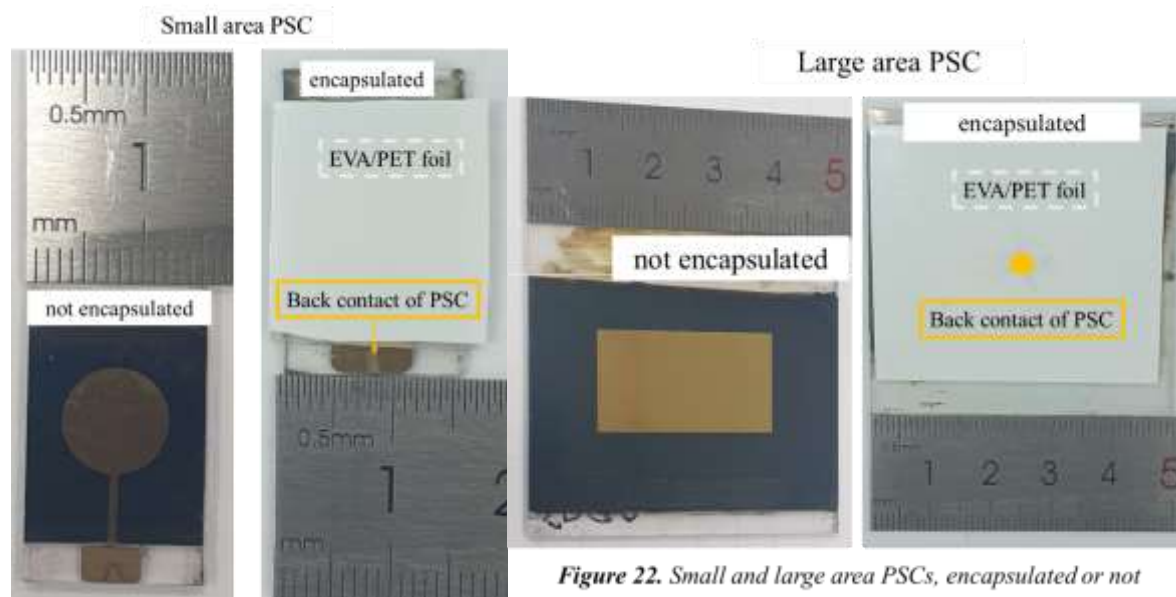


*Figure 22. Small and large area PSCs, encapsulated or not*

Details on the exploitation and dissemination of the results and of the activities

The project activities and results obtained in 2022 were disseminated in the scientific community by presenting invited, oral or poster contributions during participation in international conferences as well as via the articles and chapter published in scientific journals and books.

**3 published Articles**
1) **Article** *Effect of chlorine and bromine on the perovskite crystal growth in mesoscopic heterojunction photovoltaic device*, Hanadi Mehdi, Lucia Nicoleta Leonat, Viorica Stancu, Hamza Saidi, Monica Enculescu, Andrei-Gabriel Tomulescu, Vasilica Toma, Ioana Pintilie, Abdelaziz Bouazizi, Aurelian Catalin Galca, published in Materials Science in Semiconductor Processing 143 (2022) 106558, https://doi.org/10.1016/j.mssp.2022.106558
2) **Article** *Partial Replacement of Dimethylformamide with Less Toxic Solvents in the Fabrication Process of Mixed-Halide Perovskite Films,* Stancu, Viorica, Andrei Gabriel Tomulescu, Lucia Nicoleta Leonat, Liliana Marinela Balescu, Aurelian Catalin Galca, Vasilica Toma, Cristina Besleaga, Sarah Derbali, and Ioana Pintilie, published in *Coatings* (2023), 13, 378. https://doi.org/10.3390/coatings13020378.
3) **Article** *Capacitive and Inductive Effects in Perovskite Solar Cells: The Different Roles of Ionic Current and Ionic Charge Accumulation,* Nicolae Filipoiu, Amanda Teodora Preda, Dragos-Victor Anghel, Roxana Patru, Rachel Elizabeth Brophy, Movaffaq Kateb, Cristina

**2 Elsevier books chapters:**
1) **Chapter 2** (pages 19-55) in **Low-Dimensional Perovskites Structure, Synthesis and Applications**, Elsevier, Editors: *Yiqiang Zhan, Mohammad Khalid, Paola Vivo and Numan Arshid*: _Fundamentals and classification of halide perovskites_, S. Derbali, V. Stancu, A. G. Tomulescu, C. Besleaga, G. A. Nemnes, I. Pintilie and M. Florea; Published: on 29 November 2022, ISBN: 9780323885225, DOI: 10.1016/B978-0-323-88522-5.00005-3
2) **Chapter 5** *(pages 153-185)* in **Low-Dimensional Perovskites Structure, Synthesis and Applications**, *Elsevier, Editors: Yiqiang Zhan, Mohammad Khalid, Paola Vivo and Numan Arshid:* **_Ab initio studies on perovskites_** Authors: T. L. Mitran, R. E. Brophy, M. Cuzminschi, N. Filipoiu, M. Kateb, I. Pintilie, A. Manolescu and G. A. Nemnes; Published: on 29 November 2022, ISBN: 9780323885225,DOI: 10.1016/B978-0-323-88522-5.00012-0

**6 participation to international Conferences and 1 to a Summer School, detailed in the "Indicators" section**

1) **Summer School**: Electron transporting bilayers for perovskite solar cells: spray coating pyrolysis of c-TiO2/m-SnO2-quantum dots, A. G. Mirea, I. D. Vlaicu, I. Pintilie, S. Derbali, F. Neatu, A. G. Tomulescu, C. Besleaga-Stan, M. Enculescu, A. C. Kuncser, M. Florea, poster during SpectroCat2022-Sumer School, 26 iunie 2022-1 iulie 2022, Normandie University, Franta. https://www.lcs.ensicaen.fr/en/articles/evenements/workshop-spectrocat/

2) **Conference**: Exploring $SnO_2$ quantum dots-based electron transport layer for perovskite solar cells, S. Derbali, A. Mirea, I. Vlaicu, A.G. Tomulescu, F. Neatu, S. Neatu, C. Besleaga, M. Florea, L. Pintilie, I. Pintilie, oral contribution 15th International Symposium on Flexible Organic Electronics (ISFOE22), 4-7 July 2022, Thessaloniki, Greece. https://www.nanotexnology.com/images/stories/food/ISFOE22_PROGRAM.pdf

3) **Conferenc**e: Triple cation mixed halide perovskite and $SnO_2$ mesoporous scaffold for solar cells, V, Stancu, L. N. Leonat, A. G. Tomulescu, A. C. Gâlcă, C. Beșleagă, V. Toma, S. Derbali, L. Bălescu, M. Florea, I. Pintilie, poster contribution IBWAP 2022, 12-15 Iulie, Constanta, Romania, pg. 54 in https://ibwap.ro/wp-content/uploads/2022/07/book-abstracts_IBWAP2022.pdf

4) **Conference**: Partial substitution with imidazolium in hybrid perovskite solar cells for stability improvement, A. G. Tomulescu, L. N. Leonat, F. Neațu, V. Stancu, V. Toma, S. Derbali, Ș. Neațu, A. M. Rostas, C. Beșleagă, R. Pătru, M. Florea, I. Pintilie, oral contribution IBWAP 2022, 12-15 Iulie, Constanta, Romania, pg. 40 in https://ibwap.ro/wp-content/uploads/2022/07/book-abstracts_IBWAP2022.pdf

5) **Conference**: *Ionic drift and accumulation in perovskite solar cells: J-V hysteresis and impedance spectroscopy,* I. Pintilie, R. Patru, C. Besleaga, A. G. Tomulescu, I. Vlaicu, A. Mirea, N. Filipoiu, A. T. Preda, D. V. Anghel, G. A. Nemnes and A. Manolescu, invited talk at GEMCMP 2022, Rome, Italy, 16-18 June 2022, https://www.mscholarconferences.com/CondensedMatterPhysics/19/home.html#

6) **Conference:** *Large- and small-signal analysis of perovskite solar cells: the roles of ionic charge accumulations and ionic currents*, N. Filipoiu, A. T. Preda, D.V. Anghel, R. Patru, A. G. Tomulescu, V. Stancu, C. Besleaga, I. Pintilie, A. Manolescu, G. A. Nemnes, oral contribution IBWAP 2022, 12-15 Iulie, Constanta, Romania, pg. 123 in https://ibwap.ro/wp-content/uploads/2022/07/book-abstracts_IBWAP2022.pdf

7) **Conference**: *Optimizing the band alignment in methylammonium lead iodide – $Cu_x Ni_{1-x}O$ interface,* N. Filipoiu, M. Cuzminschi, T. L. Mitran , D. V. Anghel, G.E. Stan, C. Besleaga, I. Pintilie, K. Torfason, A. Manolescu, G. A. Nemnes, oral presentation IBWAP 2022, 12-15 Iulie, Constanta, Romania, pg. 31 in https://ibwap.ro/wp-content/uploads/2022/07/book-abstracts_IBWAP2022.pdf
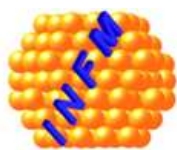
# Towards perovskite large area photovoltaics

| | |
|---|---|
| Project code: | EEA-RO-NO-2018-0106 (SEE-36) |
| Project acronym: | PERLA-PV |
| Duration: | 01.01.2021 – 31.12.2023 |
| Total budget from the Programm (euro): | 1,164,000 |
| - Grant (85%): | 989.400 |
| - Co-financing (15%): | 174.600 |
| Own budget (euro): | 545.530 |
| Project Webpage: | http://perla-pv.ro/ |
| Project Promoter organization: | INCDFM |
| Principal Investigator: | Ioana Pintilie |
| Project Partner organization (1): | Universitatea Oslo |
| Project Partner organization (2): | Universitatea Reykjavik |
| Project Partner organization (3): | IFIN-HH |
| Project Partner organization (4): | WATTROM -Tritech Group SRL |

**The EEA Grants represent the contribution of Iceland, Liechtenstein and Norway towards a green, competitive and inclusive Europe.**

**There are two overall objectives: reduction of economic and social disparities in Europe, and to strengthen bilateral relations between the donor countries and 15 EU countries in Central and Southern Europe and the Baltics.**

**The three donor countries cooperate closely with the EU through the Agreement on the European Economic Area (EEA). The donors have provided €3.3 billion through consecutive grant schemes between 1994 and 2014. For the period 2014-2021, the EEA Grants amount to €1.55 billion. The priorities for this period are: 1) Innovation, Research, Education and Competitiveness; 2) Social Inclusion, Youth Employment and Poverty Reduction; 3) Environment, Energy, Climate Change and Low Carbon Economy; 4) Culture, Civil Society, Good Governance and Fundamental Rights; 5) Justice and Home Affairs**